Assimilating visible and infrared radiances in idealized simulations of deep convection

Josef Schröttle, Martin Weissmann, Leonhard Scheck, Axel Hutt

Assimilating visible and infrared radiances in idealized simulations of deep convection

Josef Schröttle *

Meteorologisches Institut, Ludwig-Maximilians Universität, Munich, Germany and Department of Geophysics, School of Earth Sciences, Tel Aviv University, Israel

Martin Weissmann

Institut für Meteorologie und Geophysik, Universität Wien, Vienna, Austria

Leonhard Scheck

Hans-Ertel Zentrum für Wetterforschung, Ludwig-Maximilians Universität, Munich, Germany

Axel Hutt

Deutscher Wetterdienst, Offenbach, Germany and Team MIMESIS, INRIA Nancy Grand Est, Strasbourg, France

**Corresponding author address:* Department of Geophysics, School of Earth Sciences, Tel Aviv University, Israel.

E-mail: josefs@mail.tau.ac.il

Early Online Release: This preliminary version has been accepted for publication in *Monthly Weather Review*, may be fully cited, and has been assigned DOI 10.1175/MWR-D-20-0002.1. The final typeset copyedited article will replace the EOR at the above DOI when it is published.

ABSTRACT

Cloud-affected radiances from geostationary satellite sensors provide the first area-wide observable signal of convection with high spatial resolution in the range of kilometers and high temporal resolution in the range of minutes. However, these observations are not yet assimilated in operational convection-resolving weather prediction models as the rapid, non-linear evolution of clouds makes the assimilation of related observations very challenging.

To address these challenges, we investigate the assimilation of satellite radiances from visible and infrared channels in idealized observing system simulation experiments (OSSEs) for a day with summer-time deep convection in central Europe. This constitutes the first study assimilating a combination of all-sky observations from infrared and visible satellite channels and the experiments provide the opportunity to test various assimilation settings in an environment, where the observation forward operator and the numerical model exhibit no systematic errors.

The experiments provide insights into appropriate settings for the assimilation of cloud-affected satellite radiances in an ensemble data assimilation system and demonstrate the potential of these observations for convective-scale weather prediction. Both infrared and visible radiances individually lead to an overall forecast improvement, but best results are achieved with a combination of both observation types that provide complementary information on atmospheric clouds. This combination strongly improves the forecast of precipitation and other quantities throughout the whole range of 8 h lead time.

Accepted for publication in *Monthly Weather Review*. DOI 10.1175/MWR-D-20-0002.1.

1. Introduction

Convective-scale data assimilation aims at improving forecasts of severe weather events, which are often related to deep convection. The prediction of these events requires not only an accurate initial state of the large-scale environmental conditions, but also knowledge on the location and structure of individual convective systems at the km-scale. Cloud-affected satellite observations from geostationary satellite sensors provide a promising source of information in this context as they reveal insights into dynamically active regions of the atmosphere (McNally 2002) and cover a large area with high spatial resolution in the range of kilometres and high temporal resolution in the range of minutes. Furthermore, clouds are an easily detectable signal of emerging convective systems that can be observed earlier than larger precipitating hydrometeors that are seen by weather radars.

Observations from different satellite channels provide very complementary information for this purpose: Water vapor infrared channels are sensitive to water and ice clouds, containing information on atmospheric humidity and temperature. The brightness temperature of clouds observed in these channels provides information on the cloud top height. Due to the absorption by water vapor these channels peak fairly high, so they are only sensitive to mid- and upper-level clouds. Infrared window channels can see through the atmosphere, but low clouds are often hard to distinguish from the surface in these observations. Also, high-level ice clouds are often opaque in infrared channels leading to a lack of information on water clouds beneath them. Visible channels are available only during day time. While visible channels are not sensitive to temperature, humidity and cloud top height and less sensitive to ice clouds, they can provide more information on low-and mid-level clouds. Visible channels allow for a clear distinction between low-level clouds and the surface (Heinze et al. 2017), unless the latter is covered by snow or ice.

Accepted for publication in *Monthly Weather Review*. DOI 10.1175/MWR-D-20-0002.1.

Despite this wealth of available information, cloud-affected visible and infrared satellite observations are not yet assimilated in operational convection-permitting numerical weather prediction (NWP) models (Gustafsson et al. 2018; Geer et al. 2018). Previous case studies highlighted the potential benefit of assimilating cloud-affected infrared satellite observations for the prediction of tropical cyclones (Zhang et al. 2016; Otkin et al. 2017; Honda et al. 2018) and organized convection (Cintineo et al. 2016; Zhang et al. 2018, 2019) over the continental U.S. using convection-permitting models. To improve the prediction of local severe weather, infrared radiances were assimilated above the pacific (Sawada et al. 2019) with 10-min temporal resolution. Scheck et al. (2020) conducted the first study assimilating a visible satellite channel in a regional model for two cases with summertime convective precipitation over Germany. The simultaneous assimilation of visible and infrared channels has not been investigated so far. Furthermore, the impact of these two observation types on the practical predictability of precipitation has not been compared, yet.

The incorporation of cloud-affected microwave satellite radiances in global assimilation systems has led to significant forecast improvements in recent years (Bauer et al. 2010; Geer et al. 2010, 2017, 2018), but cloud-affected infrared observations are still not assimilated directly yet and microwave channels are not available on current geostationary satellites. Polar orbiting satellites, however, do not provide sufficient temporal resolution and coverage for convective-scale data assimilation in regional models.

Challenges for the assimilation of cloud-affected radiances include the errors of forward operators (Scheck et al. 2018), correlated observation errors (Janjić et al. 2017), the non-Gaussian distribution of errors (Geer et al. 2010), systematic errors in the representation of clouds (Otkin et al. 2018) and the ambiguity of observed integrated radiation in one channel resulting from the sensitivity to various model variables (e.g. water clouds, ice clouds, humidity and temperature). Various methods have been developed to address these challenges. For instance, cloud-dependent

Accepted for publication in *Monthly Weather Review*. DOI 10.1175/MWR-D-20-0002.1.

error models (Geer et al. 2010) are capable to address the non-Gaussianity of errors. Meanwhile, the error model initiated by Geer et al. (2010) has been extended for the assimilation of cloud-affected infrared radiances by Harnisch et al. (2016) and Okamoto et al. (2014). All these error models are based on error climatologies as functions of cloud impact. The error climatology typically increases with cloud impact. A different approach is the error model with dynamic observation error inflation developed by Minamide and Zhang (2017). Observation thinning mitigates issues due to correlated errors (see e.g. Waller et al. 2016), and recent studies tested the incorporation of correlated observation errors in data assimilation (Geer 2019). Observational ambiguities may be mitigated through the combined assimilation of different channels or observation types.

To investigate the potential impact of satellite data assimilation and various approaches for their treatment, Houtekamer and Zhang (2016) suggested to study the optimal use of cloud-affected radiance measurements in observing system simulation experiments (OSSEs). In an OSSE, a model simulation is regarded as truth (nature run) and several data assimilation experiments with synthetic observation simulated from the nature run are conducted that aim to reproduce the nature run as closely as possible. While Zhang et al. (2016) assimilated cloud-affected radiances in the infrared with an OSSE, Cintineo et al. (2016) combined infrared and radar observations in OSSEs. The complex configuration of their OSSE includes, e.g., structured terrain and boundary conditions from global scale model ensembles.

To reduce the complexity and focus on a particularly challenging case with randomly located convection, we conduct a more idealized OSSE with homogeneous initial conditions and small random noise to trigger convection following studies for radar data assimilation (Lange and Craig 2014; Bachmann et al. 2019, 2020). In this setup, we neglect orography and land-surface heterogeneity. The boundary and initial conditions are perturbed randomly and the statistics of the perturbations can be reproduced for even larger ensembles without requiring boundary, or initial

Accepted for publication in *Monthly Weather Review*. DOI 10.1175/MWR-D-20-0002.1.

conditions from larger scale numerical weather prediction models. Our OSSEs are based on the Payerne sounding measured over Switzerland during a day of deep convection. The convective clouds evolve throughout the the troposphere in a time scale of $\lessapprox 1/2\,\mathrm{h}$. Without topographic features, there is no preferential place where deep convection sets in (Bachmann et al. 2019), which makes the prediction of convection as well as the assimilation of related observations even more challenging.

For data assimilation, we use the local ensemble transform Kalman filter (LETKF; Hunt et al. (2007)) implemented in the km-scale ensemble data assimilation system KENDA for the operational regional model COSMO (Consortium for Small-scale Modeling) of Deutscher Wetterdienst (Schraff et al. 2016). The COSMO-KENDA system is operational at Deutscher Wetterdienst and has been used for a number of assimilation studies (Schomburg et al. 2015; Necker et al. 2018; Sommer and Weissmann 2014, 2016; Hutt et al. 2020). To calculate synthetic infrared satellite observations from the model state, we simulate the cloud-affected infrared radiances with the radiative transfer code RTTOV (Saunders et al. 1999; Matricardi and Saunders 1999). For synthetic observations in the visible channel, we use the method MFASIS (Method for FAst Satellite Image Simulation) recently put forward by Scheck et al. (2016, 2018), which is by now also included in RTTOV. Compared to the assimilation of conventional observations (Schraff et al. 2016; Necker et al. 2018), a larger number (> 6000) of all-sky radiance measurements can be assimilated every hour in a model domain covering, e.g., central Europe.

Based on these OSSEs, we compare the impact of assimilating cloud-affected radiances from an infrared water vapor channel and from a visible channel as well as the the combination of both types. We aim to find appropriate settings for the LETKF to assimilate all-sky satellite observations for the challenging case of deep convection and address the following questions:

Accepted for publication in *Monthly Weather Review*. DOI 10.1175/MWR-D-20-0002.1.

1. How can we efficiently assimilate cloud-affected radiances during deep convection?

2. What is the analysis and forecast impact of infrared and visible satellite radiances?

3. What is the benefit of combining the assimilation of infrared and visible radiances?

In the following, Section 2 describes the setup of our OSSEs. Sect. 3 discusses results from assimilating visible and infrared radiances and Sect. 4 the sensitivity of the results with respect to changes in the assimilation parameters. Conclusions are provided in Sect. 5.

2. Observing system simulation experiments

Nolan et al. (2013) discuss the complexity of simulating a nature run in OSSEs, when surface heat exchange, structured orography and boundary conditions of global scale numerical weather prediction are present. To reduce the complexity, we use an idealized setup with a flat domain and cyclic boundary conditions. This section explains the setup of our OSSEs, shows resulting fields from the nature run, and provides an impression of the simulations with a focus on synthetic satellite radiances.

a. COSMO-KENDA in an idealized configuration with initial perturbations

Our OSSE setup largely follows previous studies for radar data assimlation (Lange and Craig 2014; Bachmann et al. 2019, 2020) using the COSMO model version 5.3: We initialize wind, temperature and humidity with a radiosonde profile from Payerne, Switzerland on 30 July 2007 at 12 UTC and add two types of perturbation for each ensemble member to account for the uncertainty on smaller and larger scales (see below). The sounding is from a day with deep convection. Strong mesoscale convective systems formed on that day (Lange and Craig 2014) due to a high CAPE of 2200 J kg^{-1} and relatively low CIN in a vertical wind shear (see Fig. 1a of Bachmann

Accepted for publication in *Monthly Weather Review*. DOI 10.1175/MWR-D-20-0002.1.

et al. (2020)). In contrast to the studies undertaken by Lange and Craig (2014) and Bachmann et al. (2019, 2020), the starting time of the initial forecasts corresponds to the time of the radiosonde observation. The idealized setup is homogeneous in the horizontal without vegetation or orography. The model domain covers a region of $(L_x, L_y, L_z) = (396\,\mathrm{km} \times 396\,\mathrm{km} \times 22\,\mathrm{km})$ with a horizontal resolution of $\Delta x = \Delta y = \ 2\,\mathrm{km}$. The model integration time step is 6 s. The vertical resolution extends from 100 m in the lowest atmospheric layers to 800 m at the domain top and includes 50 model levels. A Rayleigh damping is applied aloft of 15 km. The model runs with cyclic horizontal boundary conditions. The Coriolis force is neglected. During the course of the day, the radiation on the Earth's surface varies with the zenith angle of the sun. In this way, the idealized setup mimics the weather situation of a typical day with deep convection and a strong influence of the diurnal cycle. A one-moment cloud microphysics scheme similiar to the one developed by Lin et al. (1983) is used, which includes cloud ice, cloud water, rain, snow and graupel hydrometeors and contains a simplified version of the parametrization of Seifert and Beheng (2001) for autoconversion, accretion and self-collection. Deep convection is represented explicitly and we do not apply a shallow convection scheme.

1) Ensemble perturbations and nature run

To represent initial and boundary condition uncertainty of a regional ensemble system, we add two types of perturbations to the Payerne sounding to form the initial conditions for the ensemble members: A vertically correlated perturbation that depends only on height, which is meant to represent the large-scale uncertainty, and grid scale noise for the uncertainty on smaller scales.

As in Lange and Craig (2014), the small-scale component consists of white noise with a standard deviation of $0.02\,\mathrm{m\,s^{-1}}$ for the vertical velocity and 0.02 K for the temperature and is limited to the lowest 100 hPa. Adding this white noise triggers the development of convective cells.

Accepted for publication in *Monthly Weather Review*. DOI 10.1175/MWR-D-20-0002.1.

The resulting cell-position is random and completely uncorrelated in space between ensemble members.

For the representation of larger scale errors, we add perturbations on the vertical profiles of the initial conditions following Bachmann et al. (2020). As the boundary conditions are cyclic, these perturbations represent both large-scale initial condition errors and boundary condition errors. We perturb the initial conditions in the vertical and add $u'_j(z)$, $v'_j(z)$ for wind, $T'_j(z)$ for temperature, and $rh'_j(z)$ for relative humidity for each ensemble member j. These perturbation profiles are each drawn from Gaussian random numbers without bias. The vertical correlation length between the perturbations is between 1 and 3 km. The standard deviations of the perturbations are $\sigma_u = \sigma_v = 0.25\,\mathrm{m\,s^{-1}}$ for wind, $\sigma_T = 0.25\,\mathrm{K}$ for temperature and $\sigma_{rh} = 2\,\%$ for relative humidity. These random perturbation profiles are added separately for each ensemble member to the initial conditions.

Due to the cyclic boundary conditions, the added random perturbations are sustained within the domain of each ensemble member and are only subject to diffusion.

The initial conditions for the nature run are constructed like the ones for the ensemble members, but using different random numbers. The nature run is a free forecast initialized at 12 UTC and will serve as the truth to calculate the errors of the assimilation experiments. The 40-member free ensemble forecasts (also initialized at 12 UTC) serve as the benchmark to evaluate the relative improvement by assimilating visible/infrared radiances.

In this simplified OSSE setup, we use both the same forecast model and forward operator for the simulated truth (nature run) and the assimilation/forecast experiments. This has the advantage to study the assimilation and potential impact of observations in the absence of systematic model, observation and operator deficiencies, which pose a severe issue for the assimilation of cloud-

Accepted for publication in *Monthly Weather Review*. DOI 10.1175/MWR-D-20-0002.1.

affected observations in real-world systems. However, this also means that the achieved impact is likely significantly larger than the impact of such observations in real data assimilation systems.

2) KENDA DATA ASSIMILATION CONFIGURATION

The KENDA assimilation system (Schraff et al. 2016) is operational at Deutscher Wetterdienst and has been used for a number of assimilation studies (Schomburg et al. 2015; Necker et al. 2018; Sommer and Weissmann 2014, 2016; Zeng et al. 2019). It is based on a local ensemble transform Kalman filter (LETKF; Hunt et al. (2007)). As in the operational setup, we use 40 ensemble members. In the OSSEs, we only assimilate synthetic satellite observations, but no conventional and radar observations that are usually assimilated in operational assimilation systems. Synthetic 6.2μm SEVIRI images (one of the water vapour channels) are calculated from the nature run using the RTTOV package (version 10) and visible 0.6μm images are generated using MFASIS. To represent observation errors, white noise is added to these synthetic satellite observations. This noise has a standard deviation of 3 K for brightness temperature and of 3 % for visible reflectances. In our setup, the pixels of the synthetic satellite images correspond to the cells of the horizontal model grid. While a diurnal variation of solar zenith angle (SZA) is taken into account in the internal radiative transport scheme for calculating heating rates, a fixed geometry with a SZA of 8°, a satellite zenith angle of 36° and a scattering angle of 152° is used for the generation of the satellite images. Furthermore, it should be noted that we also assimilate visible observations after sunset in this idealized study, whereas these observations would be limited to daytime in real systems. We regard these simplification to be justified in this idealised setup, because we are primarily interested in fundamental properties of the observations like their information content and not in practical problems related to their systematic errors or their restricted availability. Moreover, a

Accepted for publication in *Monthly Weather Review*. DOI 10.1175/MWR-D-20-0002.1.

major fraction of summertime convective precipitation does occur during daytime, where visible observations would be available.

The number of satellite observations is reduced by ”superobbing”, i.e. by averaging the satellite image on a certain length scale (see e.g. Scheck et al. 2020). For this purpose, the observation operator is called for each column of the model grid and then the results are averaged over blocks of 6 by 6 grid cells, corresponding to a superobbing scale of 12 km. Single thunderstorm cells exhibit a characteristic radius of $\approx$ 10 km during the onset of convection. The averaging area of $12 \times 12\,\mathrm{km}^2$ is therefore about the scale of the individual thunderstorm cells. In the standard data assimilation setup, we use a cycling period of 15 min, corresponding to the time interval between full disk SEVIRI scans from the standard 0° METEOSAT service. A horizontal averaging of the measurements to a scale of the storm system must be in accordance with the horizontal localization (Craig and Würsch 2013). A relatively small horizontal localization ($L_h = 32\,\mathrm{km}$) is chosen with the purpose to draw the ensemble closely to the observations as previously done for radar data assimilation (Lange and Craig 2014). For the experiments assimilating cloud-affected observations, we do not localize in the vertical as clouds reveal the convective dynamics of the whole atmospheric column. Only for the assimilation of clear-sky observations, we conducted one experiment without vertical localization and one experiment with vertical localization (a logarithmic radius of 0.3 hPa around the observation height of 350 hPa). The observation error for the visible spectral range is set to a constant value of 0.2 in the reference experiments and to 0.3 in further sensitivity experiments. For the infrared water vapor observations, a cloud-dependent dynamic error model is employed (Sect. 2.e). For the reference experiments, this leads to an assigned observation error of 1.1 K for clear-sky observations and an assigned error between 1.5 K and 6.4 K for cloud-affected observations. Furthermore, sensitivity experiments were performed with assigned errors increased by 50 %.

Accepted for publication in *Monthly Weather Review*. DOI 10.1175/MWR-D-20-0002.1.

In contrast to the assimilation experiments by Scheck et al. (2020) and Hutt et al. (2020), no multiplicative or additive inflation (Zeng et al. 2019) of the error covariance matrix is used. To conserve positivity of relative humidity, we employ saturation adjustment in the LETKF (Schraff et al. 2016). The data-assimilation begins at 20 UTC and ranges up to 5 h. We start forecasts with a lead time of 8 h for each ensemble member from the analysis after 1 h, 3 h, and 5 h of data assimilation (Fig. 1).

b. Overview of assimilation experiments and sensitivity studies

Table 1 summarizes the conducted experiments. These consist of four reference experiments that are discussed in section 3 and six further sensitivity experiments with modified settings that are discussed in section 4.

The first set of experiments compares the effect of assimilating different instruments and use a cycling period of 15 min: brightness temperature (BT) with standard error settings, the visible channel in $\mathrm{VIS}_{oe=0.2}$ with an assigned observation error (OE) of 0.2, and both observation types with these settings in $\mathrm{BT+VIS}_{oe=0.2}$. Experiment $\mathrm{BT}_{CA=0}$ assimilates clear-sky brightness temperature, only.

In sensitivity experiments, we increased the assigned observation errors by 50 % for brightness temperature in the experiment $\mathrm{BT}_{oe*1.5}$ and for visible observations in the experiments $\mathrm{VIS}_{oe=0.3}$ and $\mathrm{BT+VIS}_{oe=0.3}$. We additionally used 30 min and 60 min as cycling periods for the combined assimilation of brightness temperature and visible reflectance. Furthermore, only clear-sky brightness temperature was assimilated using vertical localization in experiment $\mathrm{BT}^{loc}_{CA=0}$.

Accepted for publication in *Monthly Weather Review*. DOI 10.1175/MWR-D-20-0002.1.

c. *Evolution of the nature run*

After the start of the nature run from the perturbed profile described in Sect. 2.a.1, it takes about 7 hours until the perturbations have grown sufficiently to develop into first convective cells at around 19 UTC. During this time a thin stratiform cloud layer is present, which forms right after the begin of the model run and quickly dissolves when convection sets in and air starts to descend between the convective cells. This cloud layer is probably only an artifact related to deficiencies in the model radiation and microphysics and we consider it not to be of relevance for the convective activity we are interested in.

In Fig. 2, hourly snapshots from the evolution of the nature run are displayed between 20 UTC and 1 UTC. The rows of Fig. 2 show brightness temperature in the $6.2\,\mu$m water vapor channel, visible reflectance in the $0.6\,\mu$m channel, column maximum of radar reflectivity, column maximum of the cloud ice mixing ratio, and column maximum of the cloud water mixing ratio, respectively (from top to bottom). The snapshots show a representative area of the convection that occurs horizontally isotropic over the whole domain. It is obvious that the brightness temperature of the high-peaking water vapor channel is strongly correlated with the cloud ice content and that the visible reflectances mostly depend on cloud water. There is also some weak contribution from ice clouds to the visible reflectance. This contribution is much weaker than the one from cloud water, because the mass of cloud ice in the atmosphere is smaller than the one of cloud water and the ice particles are larger, which reduces their effectiveness in scattering visible light (see discussion in Scheck et al. (2020)). The radar reflectivity Z indicates precipitation and is calculated based on the prognostic fields of rain, snow, and graupel following Done et al. (2004).

In the first column of Fig. 2, i.e. at 20 UTC, remnants of the stratiform cloud layer are still visible in VIS and QC, but at 21 UTC the layer has completely dissolved. In all rows we see signs

Accepted for publication in *Monthly Weather Review*. DOI 10.1175/MWR-D-20-0002.1.

of convective activity that increases in the first 2-3 hours and slowly decays afterwards. In BT and QI we see the increased formation of ice clouds in the first hours. The maxima in QI and the much smaller-scale structures in Z indicate the location of the cores of the convective cells. The latter are not clearly identifiable in the infrared images, as the relatively large-scale anvil clouds are opaque in this channel. In the visible channel the ice clouds are nearly transparent and smaller-scale water clouds below can be observed. It should be noted that this effect may be exaggerated by too weak anvil clouds in the model. Water clouds are not only present at the location of convective cores, but also further away, in some cases outside of the regions covered by anvil clouds. These water clouds are likely to be a result of gust fronts triggered by cold pools (Lange and Craig 2014; Lange et al. 2017).

d. Effect of initial perturbations on the ensemble spread

Following Bachmann et al. (2020), we added vertically correlated perturbations of wind, temperature, and relative humidity to the initial profile to represent larger scale errors. Already during the first hour of the model integration, this leads to significant deviations of CAPE and CIN in the ensemble members.

The initial perturbations enhance the spread of all prognostic variables at later times: The time when deep convection sets in varies over the ensemble members as can be seen in the ensemble mean brightness temperature fields - when a cooling sets in in the mean temperature (Fig. 3). While this cooling occured due to convection over all ensemble members within a time period of $\pm\,0.5\,\mathrm{h}$ before adding perturbations to the radiosonde profile (Bachmann et al. 2019, show the variability of the onset of precipitation), the time period is now extended to $\pm\,1.5\,\mathrm{h}$ with the vertical variability in the initial conditions (Fig. 3). The onset of the convection is more clearly seen in the visible channel. The mean reflectance of most members drops at 20 UTC from ≈ 0.7 to ≈ 0.4.

Accepted for publication in *Monthly Weather Review*. DOI 10.1175/MWR-D-20-0002.1.

The decrease in mean reflectance is due to the breakup of the stratus layer during the onset of convection. As deep convective clouds form, after 20 UTC, the brightness temperature decreases from $\approx 236\,\mathrm{K}$ to $\leq 232\,\mathrm{K}$ in all members. One ensemble member forms deep convective clouds already earlier at 16 UTC.

e. Observation error model for brightness temperature

To account for the non-Gaussianity of the first guess departures mainly caused by the presence of clouds we apply the cloud-dependent error model developed by Harnisch et al. (2016) to efficiently assimilate cloud-affected radiances. In this approach the assigned error is increased for cases in which the observed brightness temperature or its model equivalent is smaller than a limiting brightness temperature BT_{lim}, which is used to distinguish between clear-sky and cloudy situations. BT_{lim} mainly depends on the satellite channel. Here we focus on the $6.2\,\mu$m water vapour channel.

A number of parameters, such as limiting brightness temperature BT_{lim}, cloud impact C_a, and dynamic error variance σ_e^2 of the model are defined in the following. In addition, a brief overview of the error model for assimilating cloud-affected radiances in the context of convective-scale ensemble data assimilation is provided.

We consider the simulations for one satellite channel. The respective brightness temperature BT_x is calculated for each field-of-view (FOV), i.e., coordinate $(\tilde{x}, \tilde{y})$. A distribution of brightness temperatures results over all ensemble members and all FOVs. The radiative transfer model can also calculate the corresponding distribution, without the presence of clouds, i.e., without taking into account the cloud absorption and cloud induced scattering of radiation. The calculated brightness temperature for so called clear-sky radiative transfer and each field of view is BT_x^{clear}. To derive BT_{lim}, the BT_x values are grouped into classes. The member of each class G represents a certain brightness temperature BT within the respective limits $[BT_-^G, BT_+^G]$. We choose 0.1 K wide bins

Accepted for publication in *Monthly Weather Review*. DOI 10.1175/MWR-D-20-0002.1.

for each class. For all members within the class, the clear-sky brightness temperature is subtracted and the mean difference is calculated:

$$\Delta BT_x = \frac{1}{M_G} \sum_{g \in G} \left(BT_{x,g} - BT_{x,g}^{clear} \right).$$

In this way, monotonously increasing brightness temperatures are mapped to a discrete function ΔBT_x and M_G is the number of elements within the class G. The brightness temperature, where ΔBT_x decreases below a certain threshold of, e.g., -0.1 K, defines BT_{lim}. Following these definitions, BT_{lim} can be understood physically as the value, where clouds begin to affect the brightness temperature over all FOVs and all ensemble members on average by less than the chosen threshold.

When the limiting brightness temperature BT_{lim} is known, the cloud impact can be calculated. The cloud impact can be defined separately as C_x for the modeled and as C_y for the observed cloud fields:

$$C_{x,ij} = max(0, BT_{lim} - BT_{x,ij}),$$

$$C_{y,ij} = max(0, BT_{lim} - BT_{y,ij}).$$

The combination of both values gives the cloud impact

$$C_{a,ij} = (C_{x,ij} + C_{y,ij})/2.$$

i is a running index over each FOV, i.e., coordinate ($\tilde{x}$,$\tilde{y}$), and j is a running index over all ensemble members.

The cloud-impact values range from 0 K to ≈ 25 K in our simulations. The resulting cloud impact values are classified to a class K with a value of cloud impact $C_{a,ij} \in [C_a^{K-}, C_a^{K+}]$. The width of each cloud-impact class is 1 K, following Harnisch et al. (2016).

Accepted for publication in *Monthly Weather Review*. DOI 10.1175/MWR-D-20-0002.1.

The difference between measured and simulated brightness temperature values gives the so called first-guess departure (FGD) values:

$$FGD_{ij} = H(\mathbf{X}_{ij}) - Y_{ij},$$

where $\mathbf{X}$ is the model state vector, H is the forward operator, Y is the observed radiance, i is mapped to a field of view as follows: $i \mapsto (\tilde{x},\tilde{y})$; k is mapped to i and an ensemble member j as follows $k \mapsto (i, j)$.

The variance for each class K is defined as

$$\left(\sigma_e^K\right)^2 = \frac{1}{N} \sum_{k \in K} FGD_k^2,$$

where N is the number of elements in the class K. A histogram over all departures results for each class K. The members of each class are normalized with the corresponding σ_e^K. This leads to a modified FGD histogram (Fig. 4). The resulting distributions are more Gaussian and therefore more suitable for data assimilation.

Notably, the FGD histograms in the idealized deep convection are wider than the ones calculated by Harnisch et al. (2016) in their figure 4. We attribute this to the deep convective clouds that show a clear contrast to the warmer ground and the resulting strong FGDs at cloud edges. The distributions peak at small values, where either clear-sky or cloudy conditions occur in both the simulated observations as well as in the ensemble member. The error model leads to more Gaussian all-sky departures after the first cycle when the convection is not completely uncorrelated anymore between ensemble members. Small clear-sky departures occur especially in early assimilation cycles during the first hour. At later times, when clouds have formed in all ensemble members, the troposphere is more mixed. The corresponding first-guess departures of clear-sky radiances exhibit a wide range of clear-sky values also following a Gaussian.

Accepted for publication in *Monthly Weather Review*. DOI 10.1175/MWR-D-20-0002.1.

3. Results from assimilating visible and infrared radiances

This section focuses on the comparison of the four main assimilation experiments. The first one (BT) assimilates brightness temperatures in the infrared 6.2 μm channel with standard error settings, the second one ($VIS_{oe=0.2}$) visible reflectance in the 0.6 μm channel with a constant assigned error of 0.2, and the third one ($BT+VIS_{oe=0.2}$) both observation types with these error settings. Finally, experiment $BT_{CA=0}$ assimilates clear sky brightness temperature in the infrared 6.2 μm channel with standard error settings, i.e., an error of 1.1 K. The discussion of further sensitivity experiments with modified settings follows in section 4.

a. Impact during data assimilation cycling

Fig. 5 shows time series of the evolution of the mean absolute error of the LETKF mean prior (15-min forecast) during the 5-h assimilation period for cloud ice (QI), cloud water (QC), water vapor (QV), meridional wind (V), and temperature (T) of the free forecast experiment and the three assimilation experiments. In this idealized setup, the zonal wind behaves similarly to the meridional wind and is not shown in the following.

The clear-sky data-assimilation experiment $BT_{CA=0}$ assimilates 3162 observations in the first and 1257 observations in the second cycle, while all-sky experiments assimilate all available radiance observations over the whole domain. Without data assimilation, the error in all variables approximately doubles in the first 1-2 h, reaches its maximum after 1-3 h and decreases afterwards particularly for cloud water and cloud ice. This decrease is related to the decay of convection.

The three experiments with all-sky data assimilation nearly always exhibit a reduced error with respect to the free ensemble. The only exceptions are a slightly increased cloud water error in the BT experiment in the first hour and in the $VIS_{oe=0.2}$ experiment in the second hour.

Accepted for publication in *Monthly Weather Review*. DOI 10.1175/MWR-D-20-0002.1.

Generally, the BT experiment shows a more pronounced error reduction than $\mathrm{VIS}_{oe=0.2}$ in this situation dominated by randomly located and locally triggered deep convection. The only exception is the error of cloud water in the first hour, where $\mathrm{VIS}_{oe=0.2}$ shows a lower error than the BT experiment. At this early state of convection, most clouds are not high enough to influence the 6.2 µm brightness temperatures but are clearly detectable in the visible channel. The combination of both channels (BT+$\mathrm{VIS}_{oe=0.2}$) leads in most cases to an even stronger error reduction than that of the BT experiment. Overall, the BT+$\mathrm{VIS}_{oe=0.2}$ experiment clearly exhibits the lowest errors for all variables.

Vertical profiles of the mean first-guess error averaged over the 5-h assimilation period are shown (Fig. 6). The strongest reduction of wind and temperature errors occur in the upper troposphere between $z = 6$ km and 12 km. Again, the BT experiment shows a clearly more pronounced error reduction than $\mathrm{VIS}_{oe=0.2}$ and BT+$\mathrm{VIS}_{oe=0.2}$ shows slightly lower errors than the BT experiment.

The error of cloud water peaks around 4 km, corresponding to the melting level of ice, and all three assimilation experiments show a fairly similar reduction of these errors by about 20 %. For cloud ice at upper levels, however, infrared observations are more effective in reducing the error than visible observations. Furthermore, $\mathrm{VIS}_{oe=0.2}$ shows a lower reduction of humidity errors in the lowest two km. As neither observation type observes humidity at this height directly, this must be related to vertical correlations and changes to surface insolation by clouds.

The weaker error reduction in the $\mathrm{VIS}_{oe=0.2}$ experiment, compared to the BT experiment, evident in Figs.5 and 6 may be related to the lack of clear-sky temperature and humidity information in the visible range. Another possible explanation for this would be the ambiguity of the visible observations. BT observations are highly sensitive in clear air to the vertical profile of temperature. Visible reflectances contain no height information, so water and ice clouds can lead to the same signal. In a situation where both water and ice clouds are present it is thus possible that in the LETKF

Accepted for publication in *Monthly Weather Review*. DOI 10.1175/MWR-D-20-0002.1.

analysis weight is given to the ensemble members that have a cloud with the wrong phase at the right horizontal location. This ambiguity problem can be avoided when visible reflectances are assimilated together with the brightness temperatures as in the BT+VIS$_{oe=0.2}$ experiment. In this case the visible observations provide additional information about low clouds that is not present in the brightness temperature, leading to a further error reduction in BT+VIS$_{oe=0.2}$, compared to BT.

During the clear-sky assimilation experiment BT$_{CA=0}$ the impact on hydrometeors begins to be positive for cloud ice after a few hours (Fig.5). The overall impact during the data-assimilation is neutral as can be seen in the profiles in Fig. 6, except for temperature, where the impact is positive over the height of the clear-sky weighting function. The clear-sky radiances appear to correct the phase shift of the onset of convection, but miss direct corrections of hydrometeors.

Mean errors (”biases”) in all prognostic fields are already present in the free ensemble before data-assimilation: The errors arise from the unbiased initial perturbations due to non-linearity of the prognostic equations. To investigate if the assimilation leads to undesirable systematic effects, the evolution of the mean errors for wind, temperature and hydrometeors in the first guess during the 5 h of data assimilation and in the corresponding free forecast are compared in Figure 7. In all experiments, the mean error decreases or stays within the range of the error from the beginning of the data assimilation period - or within the range of the mean error of the free ensemble. For wind, temperature, cloud-ice, and water-vapor, the mean error decreases when BT or BT+VIS$_{oe=0.2}$ are assimilated. The rapid decrease in the mean error of cloud-water in the free ensemble is not reproduced sustainably in the conducted data-assimilation experiments. Assimilating clear-sky brightness temperature in BT$_{CA=0}$, the mean error is overall reduced.

A slight degradation of the order of magnitude of the mean error occurs in the cloud-ice, when only VIS is assimilated. However, it needs to be kept in mind that the assimilation experiments are very short. Thus, it is promising that Figure 7 overall indicates no significant increase of mean

Accepted for publication in *Monthly Weather Review*. DOI 10.1175/MWR-D-20-0002.1.

errors, but longer assimilation experiments over various scenarios would be required to investigate systematic effects in more detail.

b. Forecast impact

The forecast error for cloud variables, temperature T and meridional wind V is shown in Fig. 8. Overall, the forecast error reduction is fairly consistent with the error reduction during the data assimilation period. The all-sky assimilation experiments show lower forecast errors than the free forecast for all variables. This error reduction lasts throughout the whole forecast range of 7 h with the exception of temperature errors in the $\mathrm{VIS}_{oe=0.2}$ experiment that become similar to the free forecast after 5.5 h. The BT experiments shows roughly twice the error reduction of $\mathrm{VIS}_{oe=0.2}$ and $\mathrm{BT}+\mathrm{VIS}_{oe=0.2}$ shows even slightly lower errors than BT. The advantage of the combined assimilation of both channels is particularly apparent for humidity, temperature and wind. For hydrometeor errors, in contrast, the differences between BT and $\mathrm{BT}+\mathrm{VIS}_{oe=0.2}$ are fairly small. The clear-sky assimilation experiment $\mathrm{BT}_{CA=0}$ has a positive or neutral impact for all variables, except for temperature and horizontal wind after 1-2 h. There, a negative impact occurs due to the forecast at 21 UTC. In contrast, the forecast impact on temperature and horizontal wind remains positive at 23 UTC and 1 UTC (Sect. 4.b), when the temperature bias is smaller at the starting time of the forecast (Fig. 7).

As further metric, we employ the fractional skill score for precipitation forecasts following the evaluation of Bachmann et al. (2019) for idealized radar data assimilation OSSEs. The fractional skill score allows to derive a believable scale (sometimes referred to as skilful scale) for a precipitation forecasts. The results shown in (Fig. 9) are derived for a radar reflectivity threshold of 20.0 dBz. The believable scale indicates a non-random overlap of precipitation fields (Mittermaier and Roberts 2010) in the forecast and nature. In all our satellite data assimilation experiments, a clear

Accepted for publication in *Monthly Weather Review*. DOI 10.1175/MWR-D-20-0002.1.

reduction of the believable scale indicates improved precipitation forecasts. The believable scale increases from 100 km to 200 km in the free runs over ≤ 7 h until the rain decays (Fig. 9). The increase is due to a more and more scattered and random precipitation field. Similar to the evaluation for other forecast variables, we differentiate a clear order between the experiments from best to worst precipitation forecast as follows: Assimilating the visible channel increases the forecast skill, i.e., reduces the believable scale compared to the free background forecast at all times. The assimilation of the infrared channel leads to even better results and again, assimilating both channels is best and reduces the believable scale during the first forecasting hour to $1/4$, while resulting forecasts of the clear sky assimilation have a neutral or slightly negative impact. Assimilating the combination leads to the smallest believable scale in the forecast at the order of 10 km. This scale is close to the super-observation scale and effective model resolution.

These results are not directly comparable to the experiments for radar data assimilation by Bachmann et al. (2020) given small differences in the setup. Nevertheless, the results overall indicated that the potential impact of satellite observation is of a similar magnitude as the impact of radar observations.

Accepted for publication in *Monthly Weather Review*. DOI 10.1175/MWR-D-20-0002.1.

4. Sensitivity experiments

In this section, we discuss the sensitivity of the data assimilation experiments to modified settings of the assigned observation error and cycling frequency.

a. Sensitivity to assigned observation error

Table 2 and Fig. 10 show the effect of increasing the assigned observation error by 50 % on the forecast error of different variables averaged over lead times of 1-8 h. The improvement of the mean absolute error as depicted before is calculated relative to the free background ensemble for cloud water $\Delta QC/\Delta QC_{free}$, water vapor $\Delta QV/\Delta QV_{free}$, cloud ice $\Delta QI/\Delta QI_{free}$, horizontal wind $\Delta V/\Delta V_{free}$, and temperature $\Delta T/\Delta T_{free}$. The increased observation error leads to a lower beneficial impact for all three experiments, the experiment with observations in the visible spectrum, the experiment with infrared observations and the experiment that uses both observation types. For experiments with infrared observations and the one with both observation types, however, the difference of the experiments with increased visible observation errors to the reference experiments is fairly small. Only the experiment with visible observations shows a strong difference (overall improvement of 13 % with increased error instead of 18 % improvement in the reference experiment).

Experiments with decreased assigned observation errors either led to numerical instabilities, forecast deterioration or a very small beneficial impact (not shown). This indicates that the assigned observation error of the reference experiments is a suitable choice for the assimilation. In this context, it should also be noted that the assigned errors are strongly inflated compared to the errors used for simulating the observations. Visible observations were simulated with a random error of only 3 %. Due to superobbing of 36 pixels, the actual error is reduced further by a factor of 36 for the assimilated super-observations. This discrepancy of actual and assigned errors by more

Accepted for publication in *Monthly Weather Review*. DOI 10.1175/MWR-D-20-0002.1.

than a factor of ten is interesting given the absence of correlated observation errors and of representation and operator errors when using a model simulation as truth in an OSSE. We therefore speculate that the strong inflation of errors is necessary to compensate for displacement errors and other non-linear effects as well as for deficiencies of the data assimilation scheme. For infrared observations, the comparison of actual and assigned errors is a bit more complicated due to the use of the dynamic error model. Nevertheless, the assigned observation error of infrared observations is also strongly inflated compared to their actual observation error.

b. Sensitivity to cycling frequency & all-sky versus clear-sky brightness temperature assimilation

The cycling period was varied between 15, 30 and 60 min for the experiment assimilating the combination of infrared and visible observations with an assigned observation error of $oe = 0.2$. All experiments with lower cycling frequency are typically evaluated hourly (referred to as ”sampled hourly” in the experiment name). To study the effect of the evaluation frequency on the results, assimilation experiments with higher frequency cycling are also evaluated hourly and half-hourly. However, the error of evaluating less frequently appears to be insignificant (Fig. 11).

The comparison of the experiments with a cycling period of 1/4 h, 1/2 h, and 1 h (Table 3) reveals a larger forecast improvement for higher cycling frequencies. It is therefore beneficial to assimilate the observations with higher temporal resolution. However, the differences between the experiments are rather small despite the fact that the 1 h cycling period also decreases the amount of assimilated observations by a factor of 4 compared to the experiment with a 1/4 h cycling period. Using a 1 h cycling period may therefore be a reasonable choice if the number of assimilated observation should not be too large or if other reasons restrict the cycling period.

Assimilating only clear-sky brightness temperature observations with or without localization leads to a clear decrease in forecast skill for all variables compared to assimilating all-sky bright-

Accepted for publication in *Monthly Weather Review*. DOI 10.1175/MWR-D-20-0002.1.

ness temperature (Fig. 12). In comparison to assimilating without localization, adding localization in the clear-sky experiment $\mathrm{BT}^{loc}_{CA=0}$ can lead to a slight improvement in forecasting hydrometeors.

5. Conclusions

This paper investigates the potential impact of cloud-affected satellite observations in the visible and infrared spectrum in idealized convective-scale observing system simulation experiments (OSSEs) with a local ensemble transform Kalman filter (LETKF) for data assimilation. We investigate a particularly challenging case with locally triggered and randomly located summer-time deep convection in central Europe.

Observations from the visible and infrared channel provide very complementary information on atmospheric clouds with a higher sensitivity of the infrared channels to ice clouds and of the visible to water clouds. Furthermore, infrared channels provide information on cloud top heights whereas visible channels allow to distinguish low clouds from the surface. Despite these advantages, a combination of infrared and visible channels has not been used for data assimilation, yet.

The OSSEs demonstrate a strongly beneficial impact of satellite data assimilation on various forecast quantities for the whole forecast range of 8 h lead time. The mean relative forecast improvement ranges up to nearly 30 % for model state variables. Precipitation forecast show even more drastic improvements. The Fraction Skill Score (FSS) believable (or skilful) scale increases by up to a factor of four and means that 7-h forecasts with satellite data assimilation are better than 1-h forecasts without.

While the results are not directly comparable to the OSSE results of Bachmann et al. (2019) and Bachmann et al. (2020) for radar data assimilation due to some differences of the setup, they indicate a comparable magnitude of the potential impact of cloud-affected satellite observations to radar observations. Both visible and infrared observations individually lead to a forecast improve-

Accepted for publication in *Monthly Weather Review*. DOI 10.1175/MWR-D-20-0002.1.

ment, which is higher for infrared observations in this convective situation. Best forecast results, however, are achieved through the combined assimilation of both visible and infrared observations. We assume that this is related to the reduction of ambiguities in the observations through the combination of both types.

It should be noted that the relative effectiveness of assimilating visible or water vapor channels can be expected to depend strongly on the weather situation. For instance, when only boundary layer clouds are present, the visible channel does not suffer from a potential confusion between water and ice clouds and the water vapor channel does not contain cloud information. Therefore, we would expect a much stronger impact from the visible channel in such a case. However, the current impact on forecasts after 22 UTC does not take into account the diurnal cycle of the sun on visible observations.

Sensitivity experiments with different assigned observation errors indicate that a constant error of 0.2 for visible reflectance and of 1.1 K plus an error inflation dependent on cloud-impact based on Harnisch et al. (2016) for infrared observations is an appropriate choice. This is an interesting result given that the observations were simulated using an error of only 3 % for visible reflectance and 3 K for infrared brightness temperature observations. As the assimilated observations are super-observations consisting of 6×6 pixels, their actual error is only 1/6 of the one used for assimilating the observations. Consequently, this means that the appropriate assigned error needs to be highly inflated for the assimilation despite of the absence of correlated observation errors, representation errors, and operator errors. We assume that this strong error inflation is necessary to compensate for displacement errors and other non-linear effects as well as for deficiencies of the data assimilation scheme.

Furthermore, we conducted sensitivity experiments using cycling periods of 15, 30, and 60 min. These show that it is most beneficial to assimilate the observations every 15 min. However, a

Accepted for publication in *Monthly Weather Review*. DOI 10.1175/MWR-D-20-0002.1.

beneficial impact is also achieved using 30-min or 60-min cycling periods and given that those experiments only assimilate half or a quarter of the observations, the forecast improvement is also remarkable. Consequently, it may as well be a suitable choice to use a cycling period of 1 h for these conditions in case of need for a reduced data amount or other operational constraints.

In summary, we show than an LETKF assimilation scheme is capable of using the information provided by cloud-affected satellite observations. Their assimilation strongly improves the forecast of various quantities including precipitation. While the total impact of such observations achieved in this idealized OSSE can likely not be achieved in a real NWP system, the study provides important insights on the relative impact of observations. Best forecast results are achieved when assimilating both visible and infrared observations and overall, the impact is of comparable magnitude as the impact of radar observations. This strongly emphasizes the potential benefit of such observations for convective-scale NWP - especially in regions on the globe where a dense network of conventional observations or other remote sensing measurements are unavailable.

Acknowledgments. This study was carried out in the Hans-Ertel Centre for Weather Research (Weissmann et al. 2014; Simmer et al. 2016), which is a German research network of universities, research institutes and Deutscher Wetterdienst funded by the BMVI (Federal Ministry of Transport and Digital Infrastructure). We thank three anonymous referees for constructive suggestions on the manuscript. Furthermore, we acknowledge H. Lange and K. Bachmann for providing an earlier version of the experimental setup and R. Faulwetter for support with RTTOV.

References

Bachmann, K., C. Keil, G. C. Craig, M. Weissmann, and C. A. Welzbacher, 2020: Predictability of deep convection in idealized and operational forecasts: Effects of radar data assimilation, orography and synoptic weather regime. *Mon. Wea. Rev.*, **148 (1)**, 63–81.

Accepted for publication in *Monthly Weather Review*. DOI 10.1175/MWR-D-20-0002.1.

Bachmann, K., C. Keil, and M. Weissmann, 2019: Impact of radar data assimilation and orography on predictability of deep convection. *Quart. J. Roy. Meteor. Soc.*, **145 (718)**, 117–130.

Bauer, P., A. J. Geer, P. Lopez, and D. Salmond, 2010: Direct 4D-Var assimilation of all-sky radiances. Part I: Implementation. *Q. J. R. Meteorological Society*, **136 (652)**, 1868–1885.

Cintineo, R. M., J. A. Otkin, T. A. Jones, S. Koch, and D. J. Stensrud, 2016: Assimilation of synthetic GOES-R ABI infrared brightness temperatures and WSR-88D radar observations in a high-resolution OSSE. *Mon. Wea. Rev.*, **144 (9)**, 3159–3180.

Craig, G. C., and M. Würsch, 2013: The impact of localization and observation averaging for convective-scale data assimilation in a simple stochastic model. *Quart. J. Roy. Meteor. Soc.*, **139 (671)**, 515–523.

Done, J., C. A. Davis, and M. Weisman, 2004: The next generation of NWP: Explicit forecasts of convection using the Weather Research and Forecasting (WRF) model. *Atmos. Sci. Lett.*, **5 (6)**, 110–117.

Geer, A., and Coauthors, 2017: The growing impact of satellite observations sensitive to humidity, cloud and precipitation. *Quart. J. Roy. Meteor. Soc.*, **143 (709)**, 3189–3206.

Geer, A. J., 2019: Correlated observation error models for assimilating all-sky infrared radiances. *Atmos. Meas. Tech.*, **12 (7)**, 3629–3657.

Geer, A. J., P. Bauer, and P. Lopez, 2010: Direct 4D-Var assimilation of all-sky radiances. Part II: Assessment. *Quart. J. Roy. Meteor. Soc.*, **136 (652)**, 1886–1905.

Geer, A. J., and Coauthors, 2018: All-sky satellite data assimilation at operational weather forecasting centres. *Quart. J. Roy. Meteor. Soc.*, **144 (713)**, 1191–1217.

Accepted for publication in *Monthly Weather Review*. DOI 10.1175/MWR-D-20-0002.1.

Gustafsson, N., and Coauthors, 2018: Survey of data assimilation methods for convective-scale numerical weather prediction at operational centres. *Quart. J. Roy. Meteor. Soc.*

Harnisch, F., M. Weissmann, and Á. Periáñez, 2016: Error model for the assimilation of cloud-affected infrared satellite observations in an ensemble data assimilation system. *Quart. J. Roy. Meteor. Soc.*, **142 (697)**, 1797–1808.

Heinze, R., and Coauthors, 2017: Large-eddy simulations over Germany using ICON: a comprehensive evaluation. *Quart. J. Roy. Meteor. Soc.*, **143 (702)**, 69–100.

Honda, T., and Coauthors, 2018: Assimilating all-sky Himawari-8 satellite infrared radiances: A case of typhoon Soudelor (2015). *Mon. Wea. Rev.*, **146 (1)**, 213–229.

Houtekamer, P., and F. Zhang, 2016: Review of the ensemble Kalman filter for atmospheric data assimilation. *Mon. Wea. Rev.*, **144 (12)**, 4489–4532.

Hunt, B. R., E. J. Kostelich, and I. Szunyogh, 2007: Efficient data assimilation for spatiotemporal chaos: A local ensemble transform Kalman filter. *Physica D*, **230 (1-2)**, 112–126.

Hutt, A., and Coauthors, 2020: Assimilation of SEVIRI water vapour channels with an ensemble Kalman filter on the convective scale. *Front. Earth Sci.*, **8**, 70.

Janjić, T., and Coauthors, 2017: On the representation error in data assimilation. *Quart. J. Roy. Meteor. Soc.*, **144 (713)**, 1257–1278.

Lange, H., and G. C. Craig, 2014: The impact of data assimilation length scales on analysis and prediction of convective storms. *Mon. Wea. Rev.*, **142 (10)**, 3781–3808.

Lange, H., G. C. Craig, and T. Janjić, 2017: Characterizing noise and spurious convection in convective data assimilation. *Quart. J. Roy. Meteor. Soc.*, **143 (709)**, 3060–3069.

Accepted for publication in *Monthly Weather Review*. DOI 10.1175/MWR-D-20-0002.1.

Lin, Y.-L., R. D. Farley, and H. D. Orville, 1983: Bulk parameterization of the snow field in a cloud model. *J. Climate and Applied Meteorology*, **22 (6)**, 1065–1092.

Matricardi, M., and R. Saunders, 1999: Fast radiative transfer model for simulation of infrared atmospheric sounding interferometer radiances. *Appl. Opt.*, **38 (27)**, 5679–5691.

McNally, A., 2002: A note on the occurrence of cloud in meteorologically sensitive areas and the implications for advanced infrared sounders. *Quart. J. Roy. Meteor. Soc.*, **128 (585)**, 2551–2556.

Minamide, M., and F. Zhang, 2017: Adaptive observation error inflation for assimilating all-sky satellite radiance. *Mon. Wea. Rev.*, **145 (3)**, 1063–1081.

Mittermaier, M., and N. Roberts, 2010: Intercomparison of spatial forecast verification methods: Identifying skillful spatial scales using the fractions skill score. *Weather Forecast.*, **25 (1)**, 343–354.

Necker, T., M. Weissmann, and S. Matthias, 2018: The importance of appropriate verification metrics for the assessment of observation impact in a convection-permitting modelling system. *Quart. J. Roy. Meteor. Soc.*, **140 (714)**, 1667–1680.

Nolan, D. S., R. Atlas, K. T. Bhatia, and L. R. Bucci, 2013: Development and validation of a hurricane nature run using the joint OSSE nature run and the wrf model. *J. Adv. Model. Earth Sys.*, **5 (2)**, 382–405.

Okamoto, K., A. McNally, and W. Bell, 2014: Progress towards the assimilation of all-sky infrared radiances: an evaluation of cloud effects. *Quart. J. Roy. Meteor. Soc.*, **140 (682)**, 1603–1614.

Otkin, J. A., W. E. Lewis, A. J. Lenzen, B. D. McNoldy, and S. J. Majumdar, 2017: Assessing the accuracy of the cloud and water vapor fields in the hurricane WRF (HWRF) model using satellite infrared brightness temperatures. *Mon. Wea. Rev.*, **145 (5)**, 2027–2046.

Accepted for publication in *Monthly Weather Review*. DOI 10.1175/MWR-D-20-0002.1.

Otkin, J. A., R. Potthast, and A. S. Lawless, 2018: Nonlinear bias correction for satellite data assimilation using Taylor series polynomials. *Mon. Wea. Rev.*, **146 (1)**, 263–285.

Saunders, R., M. Matricardi, and P. Brunel, 1999: An improved fast radiative transfer model for assimilation of satellite radiance observations. *Quart. J. Roy. Meteor. Soc.*, **125 (556)**, 1407–1425.

Sawada, Y., K. Okamoto, M. Kunii, and T. Miyoshi, 2019: Assimilating every-10-minute himawari-8 infrared radiances to improve convective predictability. *J. Geophys. Res.*, **124 (5)**, 2546–2561.

Scheck, L., P. Frèrebeau, R. Buras-Schnell, and B. Mayer, 2016: A fast radiative transfer method for the simulation of visible satellite imagery. *J. Quantit. Spectrosc. Radiat. Transf.*, **175**, 54–67.

Scheck, L., M. Weissmann, and L. Bach, 2020: Assimilating visible satellite images for convective scale weather prediction: A case study. *Quart. J. Roy. Meteor. Soc.*, accepted, doi:https://doi.org/10.1002/qj.3840.

Scheck, L., M. Weissmann, and B. Mayer, 2018: Efficient methods to account for cloud-top inclination and cloud overlap in synthetic visible satellite images. *J. Atmos. Oceanic Technol.*, **35 (3)**, 665–685.

Schomburg, A., C. Schraff, and R. Potthast, 2015: A concept for the assimilation of satellite cloud information in an ensemble Kalman filter: single-observation experiments. *Quart. J. Roy. Meteor. Soc.*, **141 (688)**, 893–908.

Schraff, C., H. Reich, A. Rhodin, A. Schomburg, K. Stephan, A. Periáñez, and R. Potthast, 2016: Kilometre-scale ensemble data assimilation for the COSMO model (kenda). *Quart. J. Roy. Meteor. Soc.*, **142 (696)**, 1453–1472.

Accepted for publication in *Monthly Weather Review*. DOI 10.1175/MWR-D-20-0002.1.

Seifert, A., and K. D. Beheng, 2001: A double-moment parameterization for simulating autoconversion, accretion and selfcollection. *Atmos. Res.*, **59**, 265–281.

Simmer, C., and Coauthors, 2016: HErZ: The German Hans-Ertel Centre for Weather Research. *Bull. Amer. Meteor. Soc.*, **97 (6)**, 1057–1068.

Sommer, M., and M. Weissmann, 2014: Observation impact in a convective-scale localized ensemble transform Kalman filter. *Quart. J. Roy. Meteor. Soc.*, **140 (685)**, 2672–2679.

Sommer, M., and M. Weissmann, 2016: Ensemble-based approximation of observation impact using an observation-based verification metric. *Tellus A*, **68 (1)**, 27 885.

Waller, J. A., S. P. Ballard, S. L. Dance, G. Kelly, N. K. Nichols, and D. Simonin, 2016: Diagnosing horizontal and inter-channel observation error correlations for SEVIRI observations using observation-minus-background and observation-minus-analysis statistics. *Remote Sens.*, **8 (7)**, 581.

Weissmann, M., and Coauthors, 2014: Initial phase of the Hans-Ertel Centre for Weather Research-A virtual centre at the interface of basic and applied weather and climate research. *Meteorologische Zeitschrift*, **23**, 193–208.

Zeng, Y., T. Janjić, M. Sommer, A. de Lozar, U. Blahak, and A. Seifert, 2019: Representation of model error in convective-scale data assimilation: Additive noise based on model truncation error. *J. Adv. Model. Earth Sys.*, **11 (3)**, 752–770.

Zhang, F., M. Minamide, and E. E. Clothiaux, 2016: Potential impacts of assimilating all-sky infrared satellite radiances from goes-r on convection-permitting analysis and prediction of tropical cyclones. *Geophys. Res. Lett.*, **43 (6)**, 2954–2963.

Accepted for publication in *Monthly Weather Review*. DOI 10.1175/MWR-D-20-0002.1.

Zhang, Y., D. J. Stensrud, and F. Zhang, 2019: Simultaneous assimilation of radar and all-sky satellite infrared radiance observations for convection-allowing ensemble analysis and prediction of severe thunderstorms. *MWR*, **147 (12)**, 4389–4409.

Zhang, Y., F. Zhang, and D. J. Stensrud, 2018: Assimilating all-sky infrared radiances from goes-16 abi using an ensemble kalman filter for convection-allowing severe thunderstorms prediction. *Mon. Wea. Rev.*, **146 (10)**, 3363–3381.

Accepted for publication in *Monthly Weather Review*. DOI 10.1175/MWR-D-20-0002.1.

LIST OF TABLES

Accepted for publication in *Monthly Weather Review*. DOI 10.1175/MWR-D-20-0002.1.

	Instrument	Δt_{cycle} / min	oe	oe_{vis}	start times (UTC)
BT	wv 6.2 µm	15	$oe(CA)$		21, 23, 1
$\mathrm{VIS}_{oe=0.2}$	vis 0.6 µm	15		0.2	21, 23, 1
$\mathrm{BT+VIS}_{oe=0.2}$	wv 6.2 µm, vis 0.6 µm	15	$oe(CA)$	0.2	21, 23, 1
$\mathrm{BT}_{oe*1.5}$	wv 6.2 µm	15	$1.5\,oe(CA)$		21, 23, 1
$\mathrm{VIS}_{oe=0.3}$	vis 0.6 µm	15		0.3	21, 23, 1
$\mathrm{BT+VIS}_{oe=0.3}$	wv 6.2 µm, vis 0.6 µm	15	$oe(CA)$	0.3	21, 23, 1
$\mathrm{BT+VIS}^{1/2\,h}_{oe=0.2}$	wv 6.2 µm, vis 0.6 µm	30	$oe(CA)$	0.2	1
$\mathrm{BT+VIS}^{1\,h}_{oe=0.2}$	wv 6.2 µm, vis 0.6 µm	60	$oe(CA)$	0.2	1
$\mathrm{BT}_{CA=0}$	wv 6.2 µm	15	1.1 K		21, 23, 1
$\mathrm{BT}^{loc}_{CA=0}$	wv 6.2 µm	15	1.1 K		1

TABLE 1. Overview of all data-assimilation experiments – assimilating brightness temperature (BT), visible observations (VIS), and a combination of both with observation error $oe(CA)$ depending on cloud impact in the water vapor band (Harnisch et al. 2016) and a given constant oe_{vis} for the visible spectral range. All experiments are assimilated for $\geq$ 1 h with a cycling period of 15 min, 30 min or 1 h. Forecasts of 8 h each can be started after 4 cycles for all 40 members from the analysis. The data-assimilation cycle in all experiments begins at 20 UTC. Experiment $\mathrm{BT}_{CA=0}$ assimilates only clear-sky values, while $\mathrm{BT}^{loc}_{CA=0}$ in addition localizes the innovation around the clear-sky water vapor weighting function for 6.2 µm.

Accepted for publication in *Monthly Weather Review*. DOI 10.1175/MWR-D-20-0002.1.

	Relative improvement / %					
	QC	QV	QI	V	T	Z_{BS}
$\mathrm{VIS}_{oe=0.3}$	23.0	9.4	13.0	5.3	3.1	40.8
$\mathrm{VIS}_{oe=0.2}$	26.6	13.0	17.5	7.3	5.7	46.7
BT	35.4	20.1	31.0	17.8	13.7	77.0
$\mathrm{BT}_{oe*1.5}$	34.6	19.4	29.5	16.5	9.4	60.0
$\mathrm{BT{+}VIS}_{oe=0.3}$	36.0	22.5	32.3	20.2	17.1	80.1
$\mathrm{BT{+}VIS}_{oe=0.2}$	36.1	23.5	32.4	21.1	18.5	80.0

TABLE 2. Overview of relative improvement in percent with respect to the free background forecasts for cloud water QC, water vapor QV, cloud ice QI, meridional wind V, temperature T, and believable scale Z_{BS} of column maximum radar reflectivity. The relative improvements are averaged for each experiment over the whole forecast range of 8 h taking into account three different forecasts starting at 21 UTC, 23 UTC, and 1 UTC.

Accepted for publication in *Monthly Weather Review*. DOI 10.1175/MWR-D-20-0002.1.

	Relative improvement / %					
	QC	QV	QI	V	T	Z_{BS}
$\mathrm{BT{+}VIS}_{oe=0.2}$	45.7	23.7	34.6	24.4	16.0	88.0
$\mathrm{BT{+}VIS}^{1/2h}_{oe=0.2}$	49.2	30.8	23.5	22.2	13.7	84.8
$\mathrm{BT{+}VIS}^{1h}_{oe=0.2}$	45.1	28.3	22.0	17.1	9.6	79.0
BT	44.7	19.0	31.4	18.0	6.7	47.1
$\mathrm{BT}_{CA=0}$	4.2	3.3	3.6	2.3	0.8	-6.7
$\mathrm{BT}^{loc}_{CA=0}$	5.9	3.8	4.1	2.7	1.1	-5.8

TABLE 3. Overview of relative improvement as in Table 2, but only evaluating forecasts starting at 1 UTC.

Accepted for publication in *Monthly Weather Review*. DOI 10.1175/MWR-D-20-0002.1.

LIST OF FIGURES

Accepted for publication in *Monthly Weather Review*. DOI 10.1175/MWR-D-20-0002.1.

Accepted for publication in *Monthly Weather Review*. DOI 10.1175/MWR-D-20-0002.1.

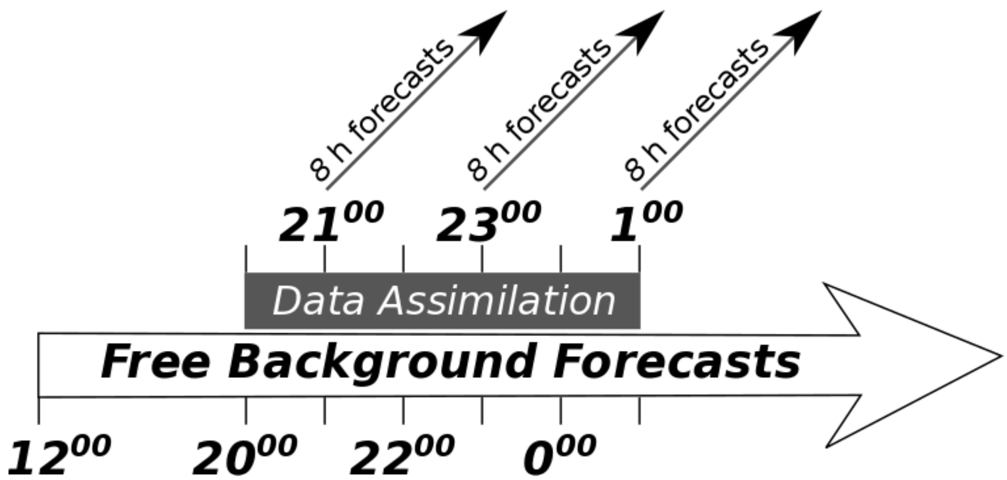

775 FIG. 1. Free background forecasts start at 12 UTC. The data assimilation provides analyses from 20 UTC
776 to 1 UTC. Forecasts of 8 hours lead time are started from the analysis at 21 UTC, 23 UTC, and 1 UTC for all
777 ensemble members.

Accepted for publication in *Monthly Weather Review*. DOI 10.1175/MWR-D-20-0002.1.

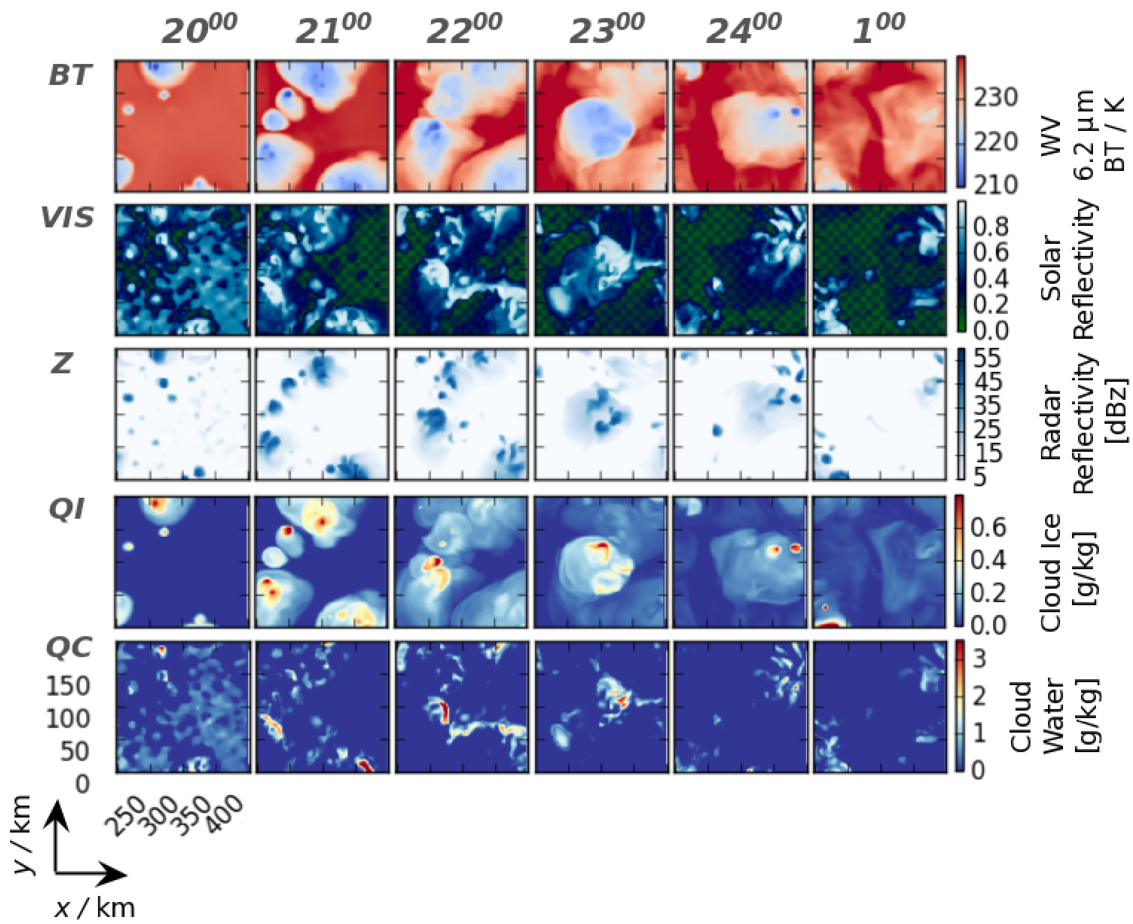

778 FIG. 2. Synthetic brightness temperature (BT) in the infrared 6.2 µm water vapor channel, reflectance in the visible 0.6 µm channel, column maximum of synthetic radar reflectivity (Z) are plotted as time series. Corresponding time series of column maximum cloud ice (QI) and column maximum cloud water (QC) are depicted below. One fourth of the domain from the nature run is shown: the south-east corner.

Accepted for publication in *Monthly Weather Review*. DOI 10.1175/MWR-D-20-0002.1.

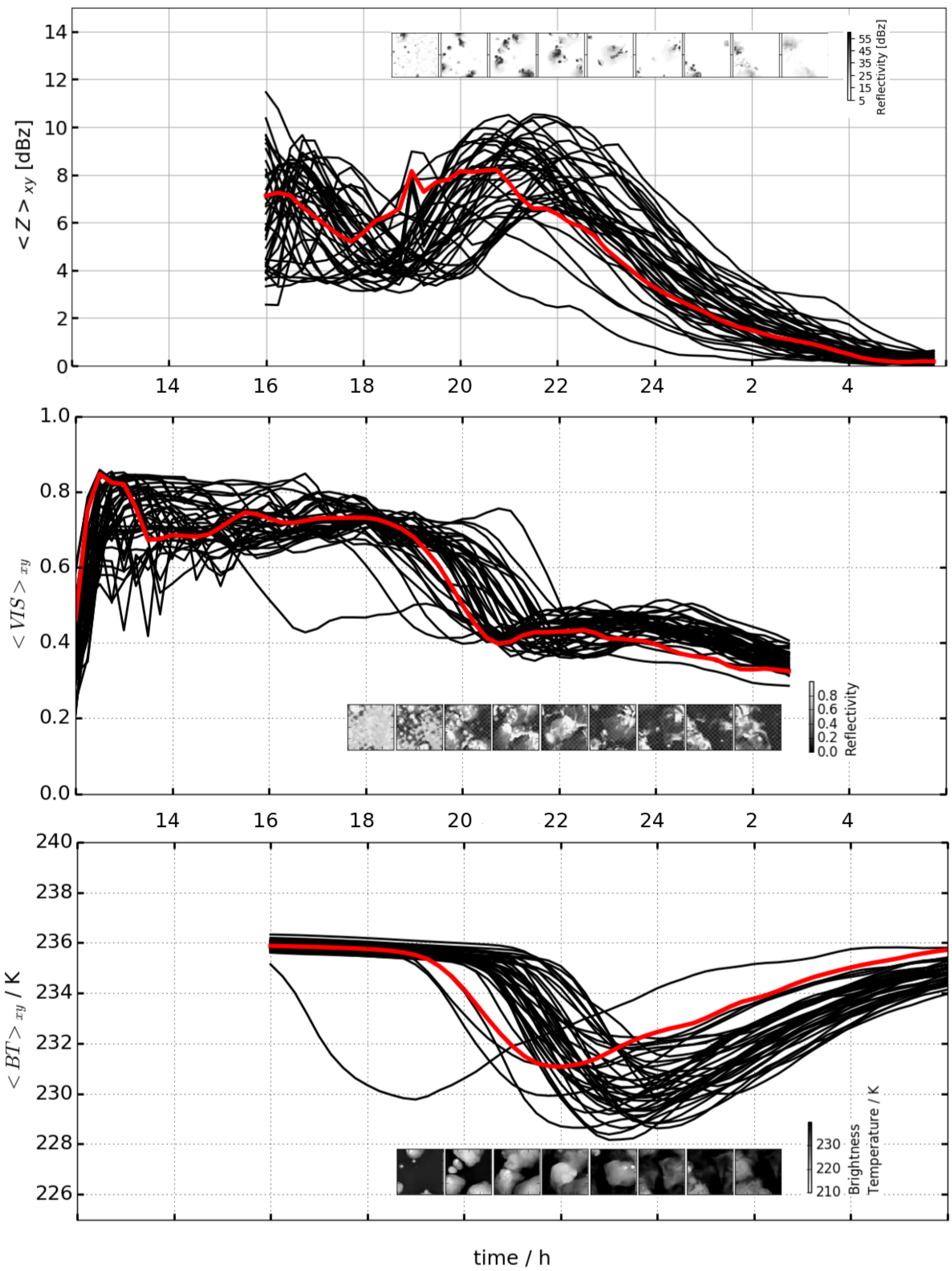

782 FIG. 3. Black lines depict horizontal means of column maximum radar reflectivity **(top)**, visible satellite
783 **(middle)**, and brightness temperature field **(bottom)** of each ensemble member. For comparison, the values
784 from the nature run are shown *(red lines)*. Corresponding fields from the previous figure are shaded in gray.
785 Brightness temperature and radar reflectivity were not stored before 16 UTC.

Accepted for publication in *Monthly Weather Review*. DOI 10.1175/MWR-D-20-0002.1.

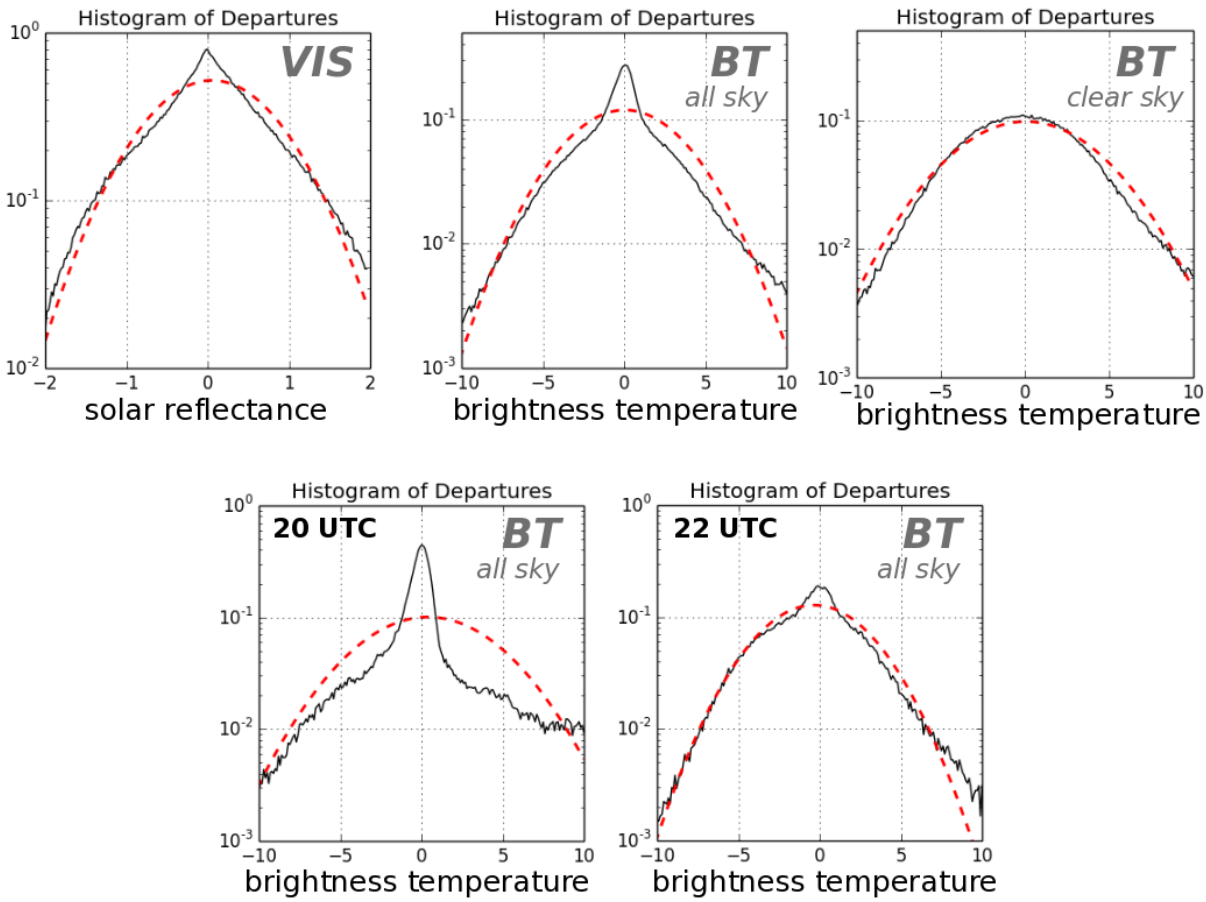

FIG. 4. First guess departures are calculated as probability density distributions for 0.8 million visible reflectance **(a)**, 0.8 million all-sky brightness temperature **(b)**, and 0.5 million clear-sky brightness temperature values **(c)** over 5 hours of assimilation time *(black lines)*. Additionally, brightness temperature all-sky departures for the first **(d)** and eighth cycle **(e)** are plotted. The values are normalized by corresponding observation errors. Corresponding bell curves are depicted with standard deviation σ_{vis} and σ_{BT} and mean μ_{vis}, $\mu_{BT} = 0$ *(dashed red lines)*.

Accepted for publication in *Monthly Weather Review*. DOI 10.1175/MWR-D-20-0002.1.

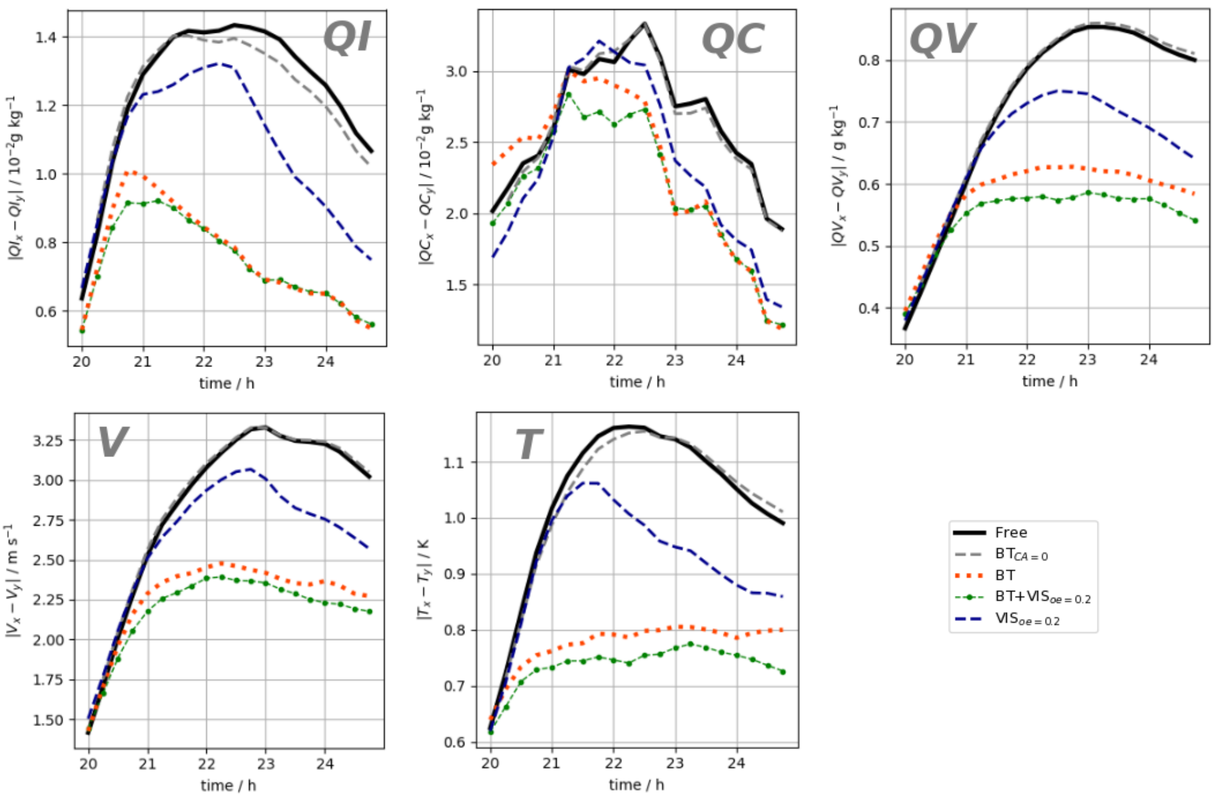

FIG. 5. Mean absolute errors of observation minus first guess averaged over the whole domain and ensemble up to a height of 15 km are shown as time series for cloud ice QI, cloud water QC, water vapor QV, meridional wind V, and temperature T (for better readability the error of QI and QC are scaled with 10^{-2}). The black line shows the error without data assimilation. Four assimilation experiments are compared: only clear-sky brightness temperature (BT$_{CA=0}$), cloud-affected brightness temperature (BT), only visible reflectances (VIS$_{oe=0.2}$) and a combination of both (BT+VIS$_{oe=0.2}$). The observation error for the cloud-affected BTs is chosen from an error model (Harnisch et al. 2016). The observation error for visible reflectances is set constant to 0.2. The free forecast *(black line)* is the mean of the 40 member ensemble forecast from the experiment without data assimilation.

Accepted for publication in *Monthly Weather Review*. DOI 10.1175/MWR-D-20-0002.1.

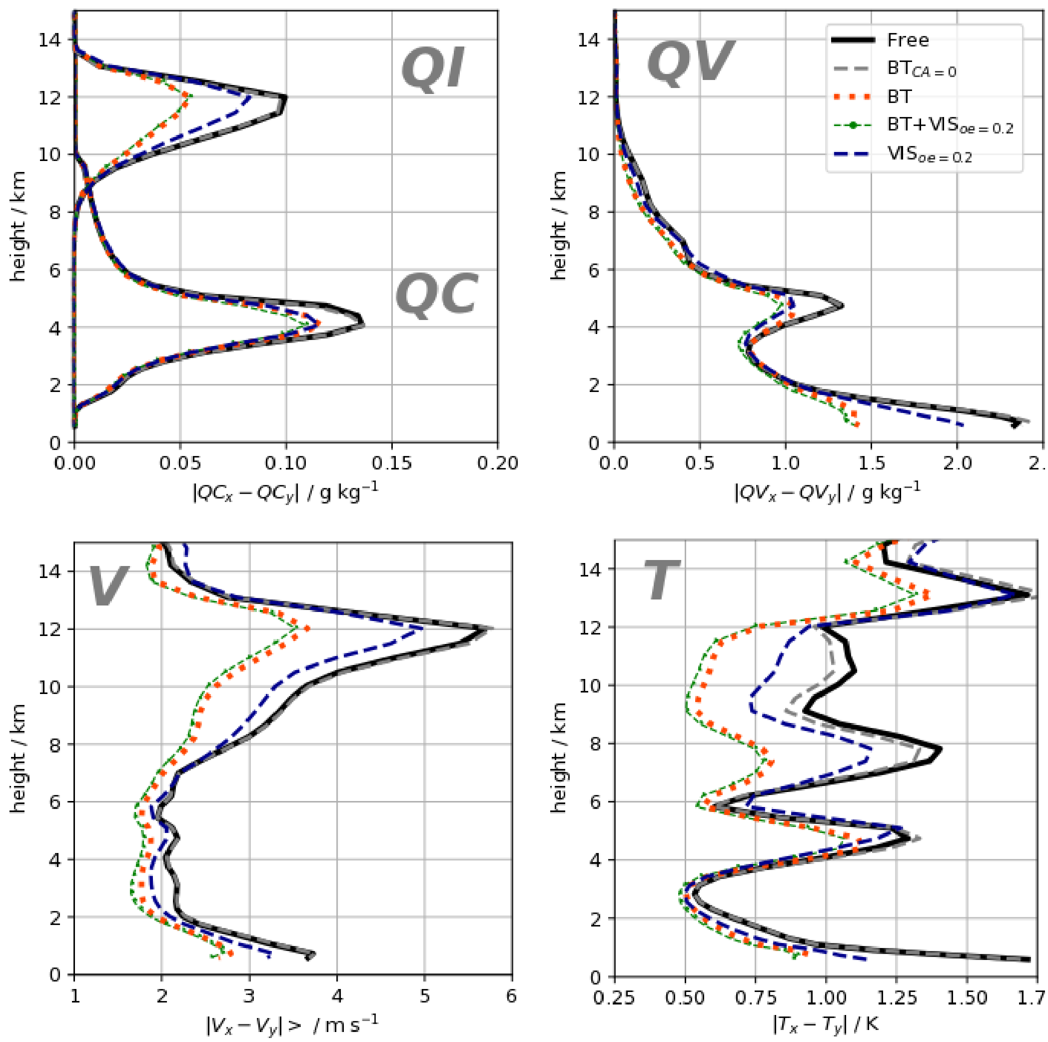

801 FIG. 6. Profiles of mean absolute error are shown of the first guess during 5 h of data assimilation. QI and QC
802 are combined in one panel. The variables and line colors correspond to the experiments in the previous figure.

Accepted for publication in *Monthly Weather Review*. DOI 10.1175/MWR-D-20-0002.1.

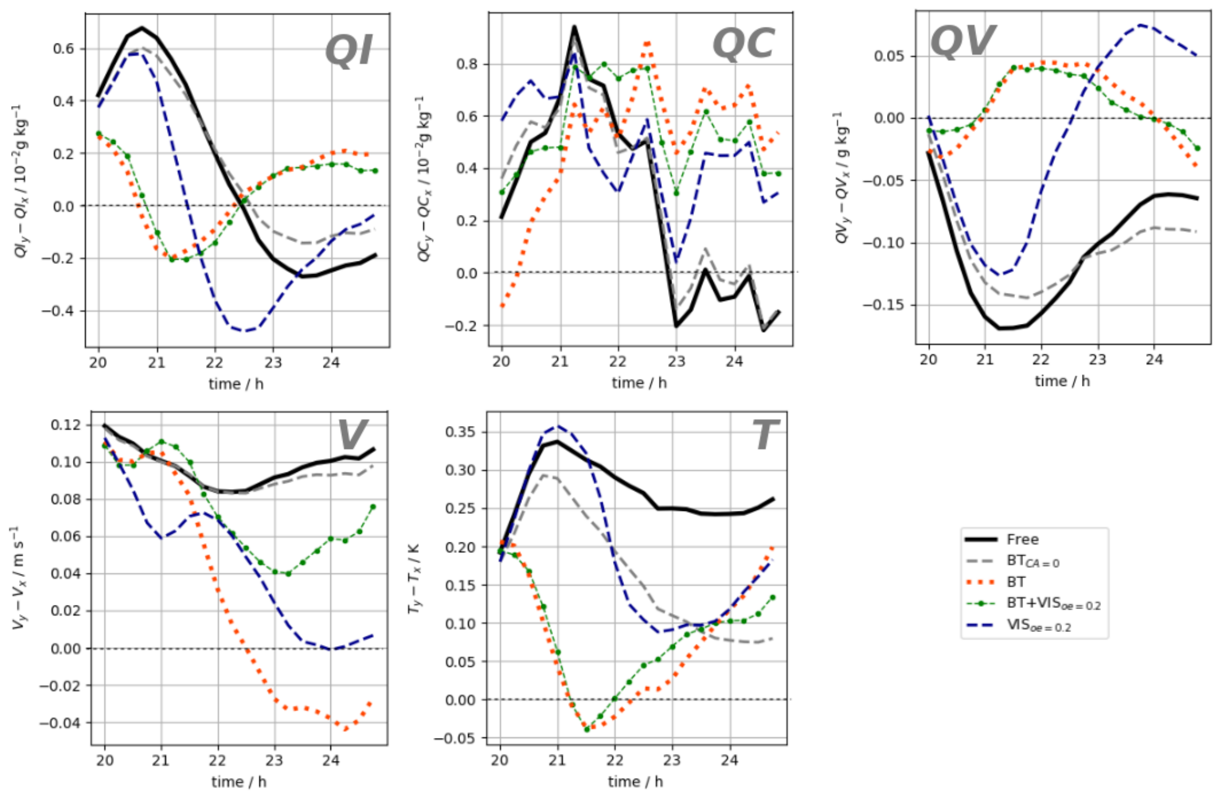

FIG. 7. Mean errors (”biases”) of observation minus first guess are shown as time series. The variables and line colors correspond to the experiments in the previous figure. For comparison the zero mean error is indicated *(thin dashed black line).*

Accepted for publication in *Monthly Weather Review*. DOI 10.1175/MWR-D-20-0002.1.

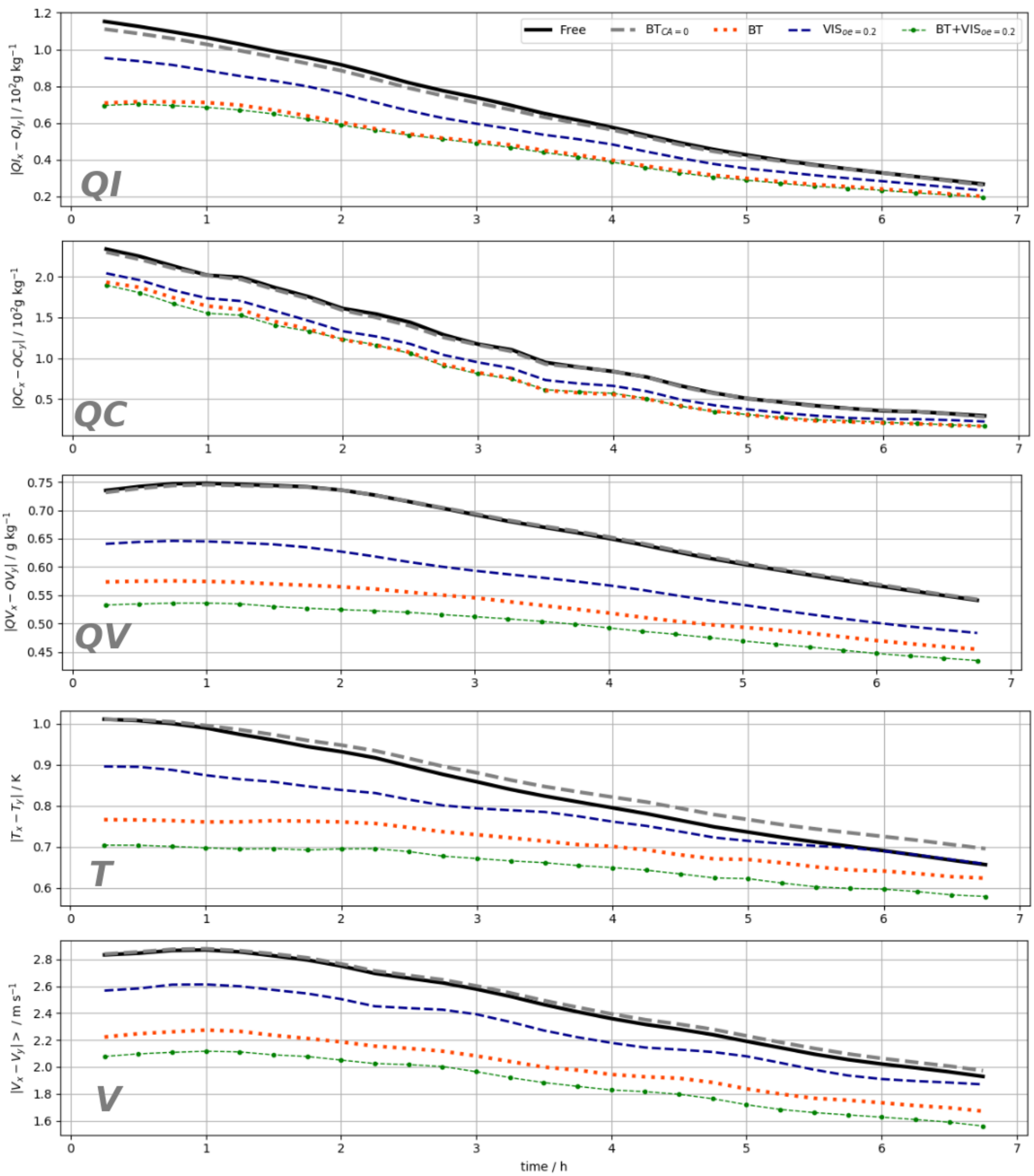

FIG. 8. Mean absolute error in forecasts of cloud ice (QI), cloud water (QC), water vapor (QV), horizontal wind (V), and temperature (T) for a set of assimilation experiments. The time series are the means over all forecast times (21 UTC, 23 UTC, 1 UTC as listed in Table 1). The line colors correspond to the experiments in the previous figures.

Accepted for publication in *Monthly Weather Review*. DOI 10.1175/MWR-D-20-0002.1.

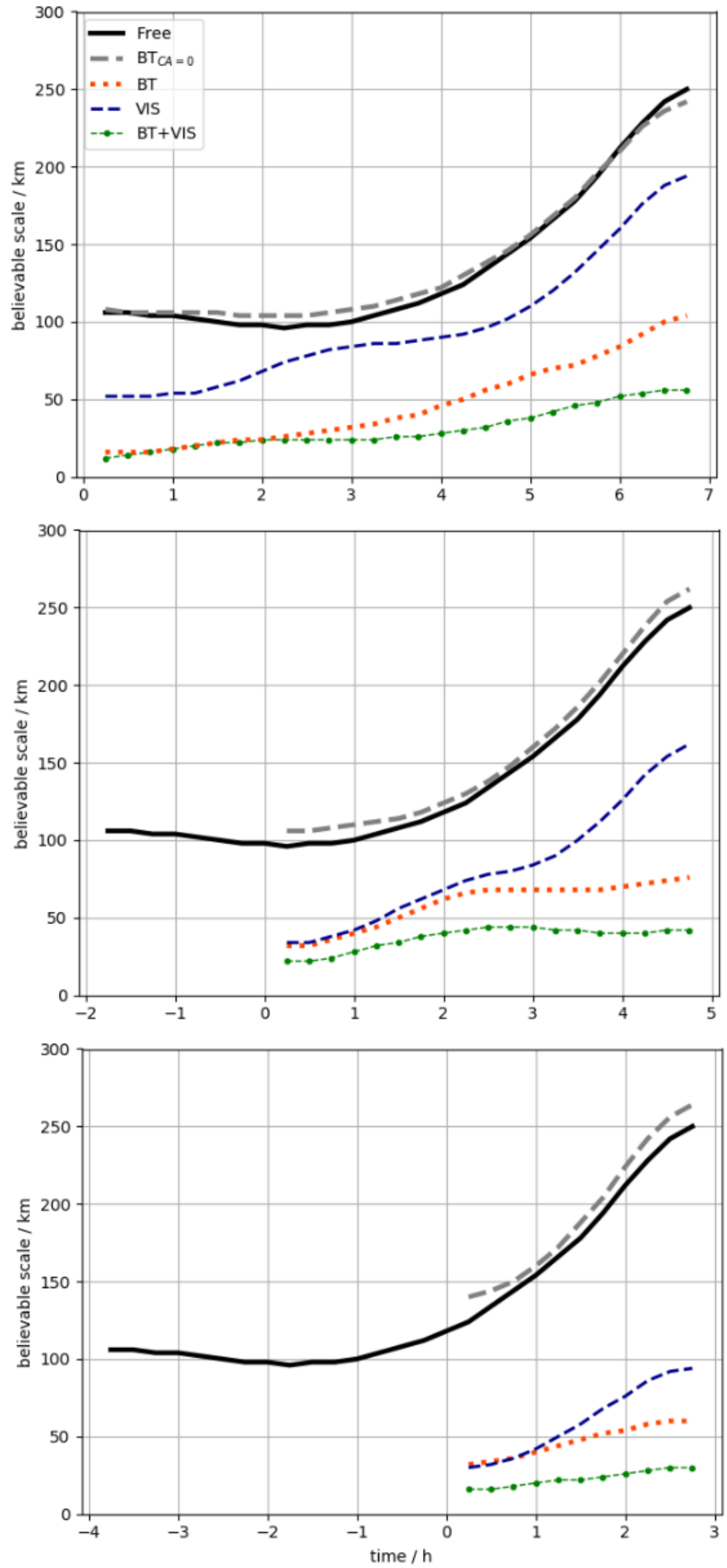

810 FIG. 9. Forecasts of the believable scale of column maximum radar reflectivity starting at 21 UTC **(top)**,
811 23 UTC **(middle)**, and 1 UTC **(bottom)**. The line colors correspond to the experiments in the previous figures.

Accepted for publication in *Monthly Weather Review*. DOI 10.1175/MWR-D-20-0002.1.

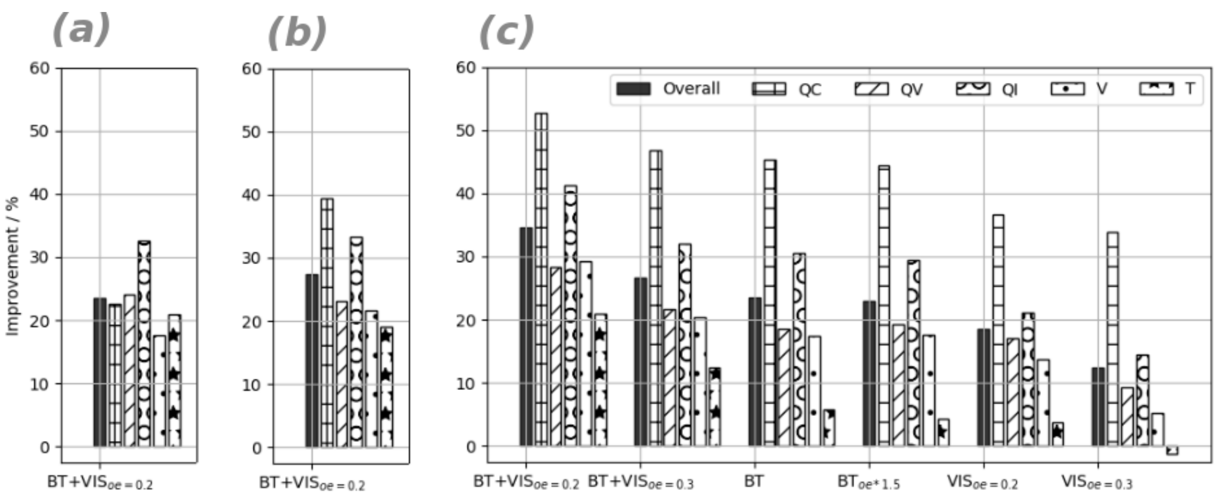

FIG. 10. Overall improvement Σ/Σ_{free} of mean relative error for (QI), cloud water (QC), water vapor (QV), horizontal wind (V) and temperature (T) for a set of assimilation experiments (Table 1). Presented is the improvement over the 8 h forecast starting at 1 UTC. All 5 variables contribute equally to the overall improvement, i.e., $\Sigma/\Sigma_{free} = (\Delta QI/\Delta QI_{free} + \Delta QC/\Delta QC_{free} + \Delta QV/\Delta QV_{free} + \Delta V/\Delta V_{free} + \Delta T/\Delta T_{free})/5$. Assimilation experiments with combined instruments $BT + VIS_{oe=0.2}$ are compared for forecasts starting at **(a)** 21 UTC, **(b)** 23 UTC, and **(c)** 1 UTC.

Accepted for publication in *Monthly Weather Review*. DOI 10.1175/MWR-D-20-0002.1.

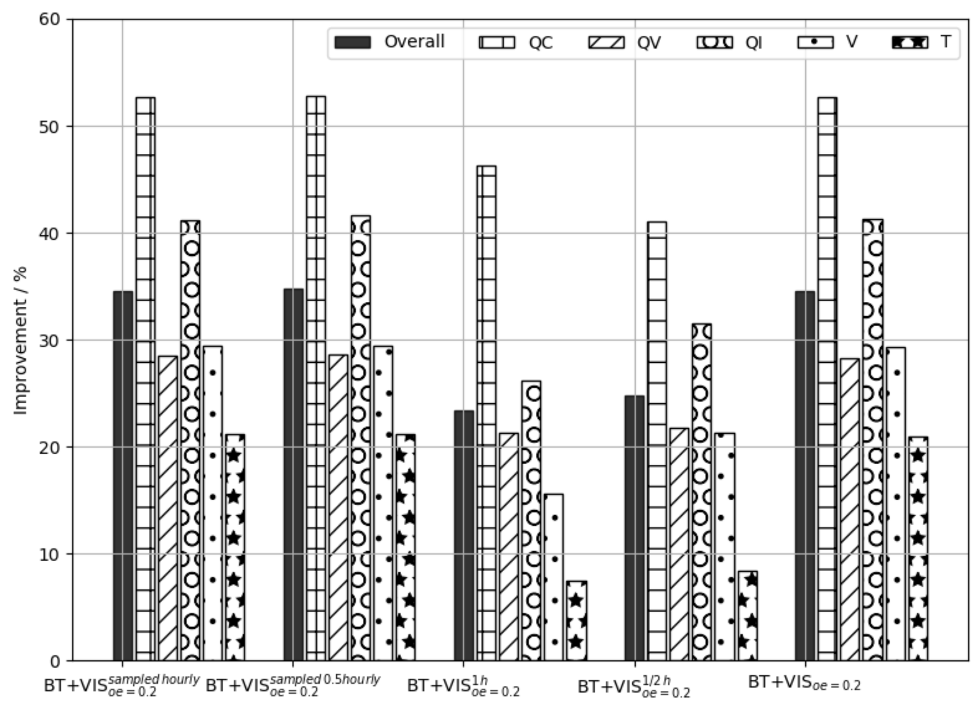

FIG. 11. As in figure 10, only varying the cycling frequency and diagnosing forecasts starting at 1 UTC.

Accepted for publication in *Monthly Weather Review*. DOI 10.1175/MWR-D-20-0002.1.

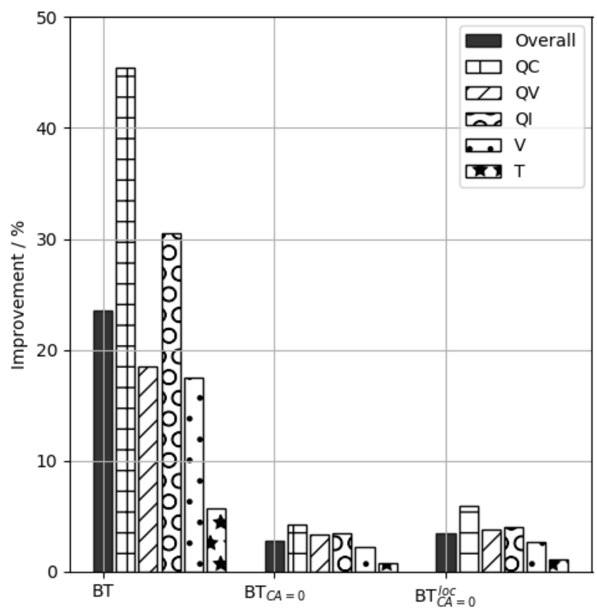

FIG. 12. Diagnosing forecasts starting at 1 UTC as in figure 11, after hourly assimilating all-sky and clear-sky brightness temperature in separate experiments.

Accepted for publication in *Monthly Weather Review*. DOI 10.1175/MWR-D-20-0002.1.